International Journal of Innovative Research and Scientific Studies, 8(6) 2025, pages: 476-488

IJIRSS
International Journal of Innovative Research & Scientific Studies

ISSN: 2617-6548

URL: www.ijirss.com

A hybrid approach with modified RCNN-based ROI identification and spot detect-X fusion strategy for DNA microarray analysis

Shreenidhi, B. S.[1*], R Saravana Kumar[2]

[1,2]*Computer Science and Engineering, Dayananda Sagar Academy of Technology and Management, Visvesvaraya Technological University, Belagavi, 590018, India.*

Corresponding author: Shreenidhi, B. S. (*Email: shreenidhibs@dsatm.edu.in*)

Abstract

As the fourth most frequent type of cancer in both men and women, lymphoid malignancies pose a significant threat to healthcare. This type of cancer has also contributed to increased mortality rates due to the inaccurate detection of diseases. To address the limitations of existing approaches, a novel method called a Hybrid Modified RCNN-based ROI Identification and Spot Detect-X Fusion Strategy for DNA microarray analysis is proposed. Initially, the data undergoes pre-processing using various techniques such as Image Augmentation, Quantile Normalization, Background Correction, and Noise Reduction with an Improved Median Filter. ROI identification is performed using the modified RCNN. Subsequently, features are extracted, and feature selection is based on the Hybrid Anaconda-based Serval Optimization. Finally, diseases are classified using the Spot Detect-X Fusion Strategy. The proposed model achieved an accuracy of 98.98% when implemented in a MATLAB platform. Therefore, the recommended model demonstrates superior performance compared to existing methods.

Keywords: Anaconda-based serval optimization, Lymphoid malignancies, RCNN, ROI identification, Spot Detect-X fusion.

DOI: 10.53894/ijirss.v8i6.9636
Funding: This study received no specific financial support.
History: Received: 8 July 2025 / **Revised:** 11 August 2025 / **Accepted:** 14 August 2025 / **Published:** 3 September 2025

Competing Interests: The authors declare that they have no competing interests.
Authors' Contributions: Both authors contributed equally to the conception and design of the study. Both authors have read and agreed to the published version of the manuscript.
Transparency: The authors confirm that the manuscript is an honest, accurate, and transparent account of the study; that no vital features of the study have been omitted; and that any discrepancies from the study as planned have been explained. This study followed all ethical practices during writing.
Publisher: Innovative Research Publishing

1. Introduction

The interaction of tumours with their surrounding microenvironment (TME) is crucial for the growth and progression of cancer. The TME comprises various cell types, including immune cells and fibroblasts. The host immune system plays a vital role in controlling tumour development by initiating inflammatory responses and maintaining immune surveillance. A substantial body of data indicates that tumour-infiltrating lymphocytes (TILs) are present within the TME, and their spatial distribution holds significant relevance for both diagnostic and predictive purposes across different cancer types [1]. As the fourth most prevalent malignancy in both sexes, lymphoid malignancies pose a serious threat to healthcare. Globally, diffuse large B-cell lymphoma is the most frequent lymphoma category, accounting for 40% of all non-Hodgkin lymphomas [2].

The distinctive feature of follicular lymphoma (FL) is a recurrent chromosomal translocation that merges the IGH and BCL2 genes. As these cells re-enter the germinal center (GC) pathway, this occurrence in early pre-B cells in the bone marrow may cause FL development. However, a recurrent translocation linked to Cyclin-D1 dysregulation is associated with Mantle Cell Lymphoma (MCL) [3, 4]. Small lymphocytic lymphoma (SLL) and chronic lymphocytic leukemia (CLL) are examples of mature B cell neoplasms characterized by the slow accumulation of monoclonal B cells. SLL is primarily involved in lymph nodes, whereas CLL predominantly affects the blood; however, their clinical and immunological features are identical. CLL is the most common leukemia in Western countries and often presents as painless lymphadenopathy or remains asymptomatic. A small percentage of patients may exhibit classic lymphoma symptoms, including fever, fatigue, night sweats, and unexplained weight loss [5].

Accurate histopathological analysis remains essential for identifying the clinically and physiologically heterogeneous subset of lymphoid cancers [6]. Thanks to developments in DNA microarray technology, researchers can now evaluate the expression of hundreds of genes simultaneously in a single experiment [7]. Gene expression profiling using microarray technology is a useful tool for managing cancer treatment and providing a prognosis. Tens of thousands of genes may be examined for each data point thanks to this technique, which helps to clarify the levels of genetic expression [8]. While many individuals with lymphoid malignancies may not show any symptoms, some may develop autoimmune problems, acquired immune deficiency syndromes, or classic lymphoma signs. Blood tests that show elevated lymphocyte counts are usually used for diagnosis; peripheral blood smears and flow cytometry are then used to confirm the illness. Deep learning, a kind of automated learning based on neural networks, has gained popularity recently for its remarkable accuracy in identifying illnesses from medical imaging. Several models and algorithms are available to aid in the identification and diagnosis of different diseases. Previous research in pathology has shown that deep learning models may perform as well as human specialists in diagnostic tasks like tumor identification and histologic grading. Deep learning-based techniques have a number of advantages over earlier systems that relied on manually built features. Firstly, they can automatically discover prognostic characteristics, which removes the requirement for presumptions or dependence on a small number of known features [9-11]. The main contribution of the research is as follows,

- Pre-processing is done by various methods along with the Improved median filter
- ROI identification is done using the modified RCNN.
- Feature selection is based on the Hybrid Anaconda-based serval optimization.
- Spot Detect-X Fusion Strategy is employed for Classification

The rest of the paper includes Related works, Recommended model, Results and Discussions, and Conclusion in the Sections 2,3,4 and 5.

2. Related Works

Chandana et al. [12] used radial basis function and multilayer perceptron machine learning algorithms to precisely categorize lymphoma subtypes and predict patient survival. It highlighted the significance of immuno-oncology markers associated with tumor-associated macrophages (TAMs) and regulatory T lymphocytes (Tregs), such as CD163, CSF1R, PD-L1, and FOXP3. Additionally, the study examined gene prognostics and their relationship to immunological pathways, emphasizing the importance of these findings for the prognosis and management of neoplasms.

Colombo et al. [13] examined the use of imaging mass cytometry (IMC) in diffuse large B-cell lymphoma (DLBCL) has been examined to analyze the tumor microenvironment (TME). It reveals anatomical and functional differences throughout the DLBCL TME, identifying unique tumor-centric subregions with a range of immune responses. Moreover, the comparison of the DLBCL TME with that of reactive lymph nodes and Hodgkin lymphoma clarifies differences in the numbers and functional conditions of immune cell subsets among different lymphoma types. Furthermore, it was possible to identify targets that may be used to increase immune cell infiltration into the tumor core areas.

Nagarathna and Kusuma [14] discussed an approach that involves using feature extraction and segmentation. The research first calculates the volume of colorectal lymphomas automatically from 3D MRI scans. Subsequently, fuzzy logic clustering and optimization techniques are employed to address the segmentation and categorization of aberrant lymph nodes. Finally, a Deep Residual Boltzmann CNN is used for classification, which enhances the accuracy of lymphoma diagnosis.

Coleman et al. [15] investigated the use of the PAM50 gene collection and algorithm to classify metastatic castration-resistant prostate tumors (mCRPC) into discrete subgroups. It distinguishes Luminal A, Luminal B, and Basal subtypes by identifying luminal and basal characteristics within mCRPCs. These subgroups are associated with certain symptoms, druggable targets, and genetic changes. The research highlights that PAM50 categorization exhibits both intratumoral and intra-individual variation, pointing to distinct phenotypic profiles. It also implies that PAM50 subgroups may have a therapeutic role in forecasting treatment outcomes and responses in individuals with mCRPC.

Preetham et al. [16] explored the use of artificial intelligence (AI) and radiogenomics in the characterization of brain tumors, emphasizing the importance of understanding genetic and molecular characteristics for accurate diagnosis and therapy. The study highlights the application of AI in identifying genetic variants from radiological images and reviews current advancements in radiomics and radiogenomics. It also ranks radiogenomics research based on AI-related parameters and assesses them for potential bias. Although AI shows promise for brain tumor research, challenges remain, such as limited access to radiomics databases and the need for precise definition of the region of interest.

Preetham and Battu [17] provided a powerful framework for identifying various cancer types by utilizing a hybrid CNN and Bi-LSTM technique to predict cancer type based on microarray gene expressions. The proposed CNN and Bi-

LSTM surpass the current CNN and LSTM classifiers in numerous performance metrics, according to the experimental results.

Malignant lymphoma classification is crucial because it ranks as the fourth most common type of cancer. Various approaches exist for the detection of such diseases. To overcome the challenges of existing methods, a novel approach should be introduced, which can be achieved by using hybrid optimization algorithms and improved classification models. This will result in higher performance in disease detection.

3. Proposed System

The data is first pre-processed using a variety of methods in which the images are augmented by flipping and rotation, quantile normalization, and background correction using the rolling ball algorithm and an improved median filter for noise reduction. The modified RCNN is used for ROI identification. The texture and shape features are then extracted, and the hybrid Anaconda-based serval optimization is used to choose the optimal features. Finally, the Spot Detect-X Fusion Strategy, which is an integration of ResNet, EfficientNet, SqueezeNet, and DarkNet-53, is employed to classify the diseases. Figure 1 shows the Suggested model.

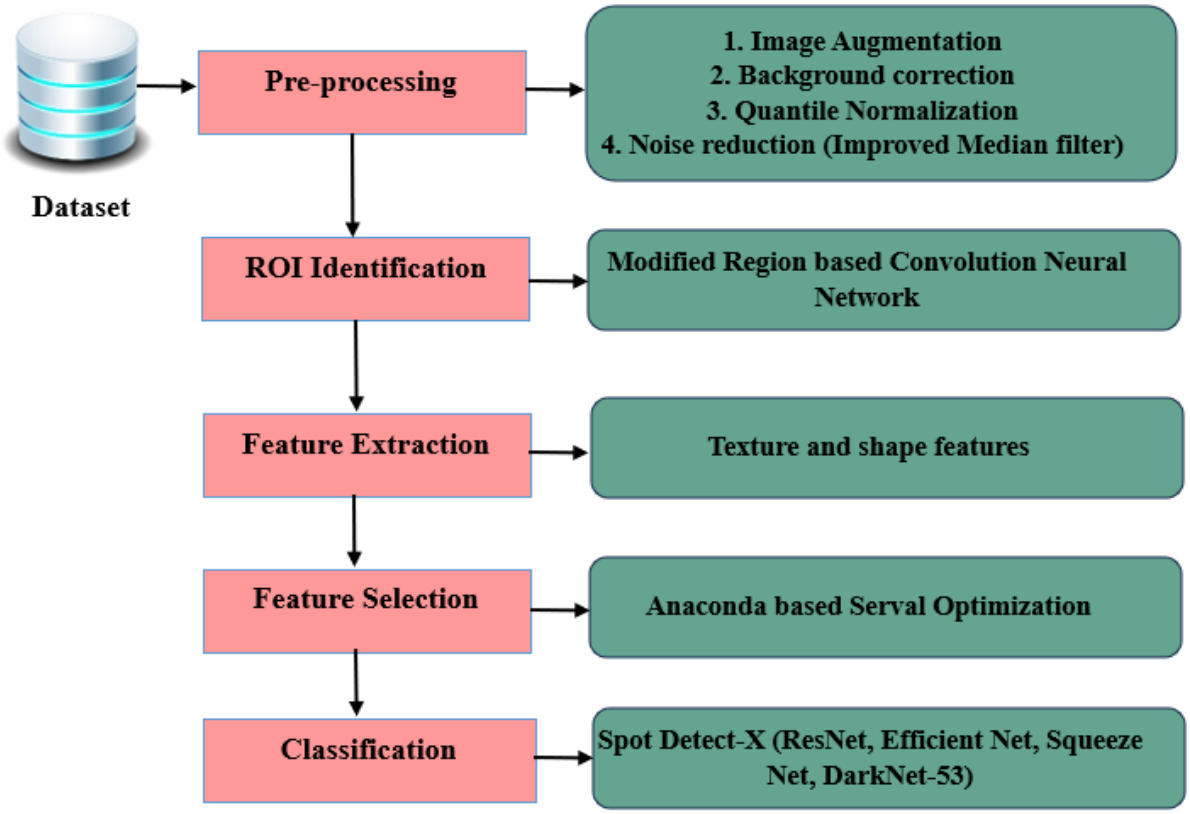

Figure 1.
Recommended model.

3.1. Pre-Processing

It is an essential step in transforming the unprocessed dataset into the ideal format. This step led to an increase in classification accuracy. The dataset can contain some noisy signals and duplicate data. The dataset has been preprocessed using the cutting-edge method described below.

3.1.1. Image Augmentation

It is a powerful technique that may be applied to artificially increase a training dataset. This can be helpful when there is insufficient data to train a model. It strengthens a model's resilience to modifications in the input data. To help the model understand invariant properties and changes in the data, transformed images are added to the dataset, enhancing the model's capacity to handle real-world situations. Some of the techniques to enhance images are rotation and flipping.

3.1.2. Background Correction

One adaptive technique for background correction that stands out is the Rolling Ball (RB) algorithm. It provides a flexible solution that is not dependent on comparisons between various pictures or time-zero or blank images. One of the most popular image processing techniques is Rolling Ball Background Subtraction (RBBS), which is used to reduce background noise or uneven lighting in images. It dramatically improves widefield (WF) image contrast, opening up a variety of possibilities for fine-tuning WF images via complex image and computational processing to reduce background noise. By computing a local background value for every pixel, which is obtained by a laborious averaging procedure across

a big ball containing the pixel, RBBS efficiently removes continuous or uneven backgrounds. This value is then deducted from the original image to provide a refined output. The rolling ball radius, which ideally matches or exceeds the radius of the largest item that is not regarded as part of the backdrop, is the key factor determining the effectiveness of RBBS. When the system's magnification is known, predicting this parameter is very simple, but accuracy decreases when sample types differ or contain unusual features.

3.1.3. Normalization

The process of structuring information within a database is called normalization. By removing superfluous information and incompatible dependencies, it protects the data and increases database flexibility, which can be done by employing a Quantile normalization. It is frequently applied to the analysis of high-dimensional data. QN is widely used and yields distributions that are remarkably well-aligned; all QN-normalized samples have identical distributions. The procedure entails sorting each gene in the sample according to its magnitude, calculating the average value for genes that are in the same rank, and then replacing the values of every gene in that specific rank with the average value. The next stage is arranging each sample's genes back in the order they were originally found.

3.1.4. Noise Reduction

One common method for attenuating noise is the nonlinear median filter technique. Improving the results of further analysis, such as edge recognition in an image, is a standard process. Its ability to fully eliminate the effect of extremely high-magnitude input noise levels gives it a considerable advantage over linear filters. They serve as filters for the removal of salt-and-pepper noise. An improved median filter algorithm is implemented for the de-noising of highly corrupted images and edge preservation, which is achieved by fusing the median filter with a Gaussian filter. The following is the process for enhancing image quality: First, the spatial noise reduction filter's mask matrix of size $n \times m$ is set. Next, for the deteriorated image corresponding to the mask pixel size, the new pixel value is recalculated using the mask matrix in comparison to the mask pixel value. Every pixel value is changed by the median filter to the median value at the center pixel that corresponds to the mask matrix. By maintaining the boundaries of the images yet blurring them, Gaussian filtering is frequently used to decrease noise in images. It works by applying a Gaussian kernel to the image through convolution. High-frequency noise, such as Gaussian noise, which is typified by erratic changes in pixel intensity, is effectively removed by this filter. The degree of smoothing may be altered by varying the kernel size, which is usually established by the standard deviation. By tuning the parameters of the window size of the median filter and the kernel size of the Gaussian filters, the noises are removed, thus resulting in an improved quality of images.

3.2. ROI Identification

Region-based Convolutional Neural Network (RCNN) with an upgraded modification is used to segregate regions inside medical images. Transfer learning may be used to train the network even in the absence of labeled input. Region proposal (RP) and bounding box (BB) are the two primary processes in the RCNN. A Region Proposal Network (RPN) handles the RP position, generating area recommendations by predicting bounding boxes for likely objects based on analysis of input images. Mapping suggestions from the Region Proposal Network (RPN) to a convolutional feature map yield Regions of Interest (ROI). ROI pooling is used to modify the bounding box sizes before the data is sent to a fully connected layer. Label scores and modified bounding box locations using the SoftMax function are included in the final findings. A hybrid optimization approach is used in the RPN optimization. There are several CNN designs that may be applied; the Path Aggregation Network (PAN) uses a bottom-up path augmentation method to overcome positional information issues. Through adaptive feature pooling, which gives each proposal access to prediction data from several layers, PANet significantly enhances performance. The overall performance is improved by these structural improvements.

The model is trained to predict the correct class, bounding box, and segmentation mask for each RP using the RCNN segmentation loss function. The segmentation mask loss guarantees that the model learns to accurately predict the shape of objects in images; the BB regression loss guarantees that the model learns to accurately predict the location and size of objects in images; and the classification loss guarantees that the model learns to distinguish between different classes of objects.

$$L = L_c + L_b + L_s \quad (1)$$

L_c is defined as the Binary Cross Entropy (BCE) loss, and it is given as,

$$L_{BCE} = (1 - y).log(1 - p) + y.log\, p \quad (2)$$

Where p, y represents the probability of BB and the corresponding label.

L_b is defined as a summation of the smooth $L1$ loss and it is defined as,

$$L_b(c, d) = \sum smooth_{L1}(c_i - d_i) \quad (3)$$

Where c represents the predicted tuple that describes the location of the bounding box,d represents the ground truth location

$$smooth_{L1}(m_i) = \begin{cases} 0.5.{m_i}^2; if\ |m_i| < 1 \\ |m_i| - 0.5; otherwise \end{cases} \quad (4)$$

Where $m_i = c_i - d_i$

L_s is the segmentation loss and it is given as,

$$L_s = BCE(f_i, g_i) \quad (5)$$

f_i is the predicted segmentation mask, g_i is the ground truth segmentation mask.

Modified RCNN is a powerful tool in medical imaging. By optimizing the RCNN, more efficient and accurate results are obtained, which will make them even more useful for a wider range of applications.

3.3. Feature Extraction

Feature extraction involves extracting new, more informative, and condensed features from the original collection. In our research, texture and shape features are extracted from the segmented results.

3.3.1. Texture-based features using Haralick

This image processing method is widely utilized for texture analysis and categorization in images by extracting texture features. The Haralick texture characteristics are computed using the Haralick () function, based on the gray-level co-occurrence matrix. This matrix $[p, q]$ dimensions of $N(g)$, where each element represents the probability of finding a pixel with value p adjacent to a pixel with value q, depending on the frequency of this comparison within the image.

$$G[p,q] = \begin{bmatrix} p(1,1) & p(1,2) & p(1,N(g)) \\ p(2,1) & p(2,1) & p(2,N(g)) \\ p(N(g),1) & p(N(g),2) & p(N(g),N(g)) \end{bmatrix} \quad (6)$$

3.3.2. Shape-Based Features

It is an important low-level feature obtained from Zernike moments, as it is helpful in the identification of real-world shapes and objects. The features produced by applying a complex set of Zernike polynomials to the input image are known as Zernike moments (ZMs). Because they are rotationally invariant, the magnitude of these moments is used for recognition. The Zernike radial polynomials are given as,

$$R_{nm}(f,g) = \sum_{s=0}^{(n-|m|)/2}(-1)^s \times \frac{(f^2+g^2)^{\frac{n-2s}{2}}(n-s)!}{s!\left(\left(n+\frac{|m|}{2}-s\right)!\left(\left(n-\frac{|m|}{2}-s\right)!\right)\right)} \quad (7)$$

n is a non-negative integer m is a nonzero integer; $n - |m|\ is\ even\ and\ |m| \leq n$

The (n, m)order of Zernike bias function is given as,

$$V_{nm}(f,g) = R_{nm}(f,g)e^{jm\theta} \quad (8)$$

Where $j = \sqrt{-1}$, $\theta = tan^{-1}\left(\frac{g}{f}\right)$

The ZMs of order *n* and repetition *m* of a function *f* (*x*, *y*) are defined by,

$$Z_{nm} = \frac{n+1}{\pi}\int_0^{2\pi}\int_0^1 f(f,g)\,V_{nm}^*(f,g)dfdg \quad (9)$$

Where $V_{nm}^*$is a complex conjugate of V_{nm}

3.3.3. Inception V3

An improved CNN architecture known as Inception V3 includes Inception modules, which typically consist of one maximum pooling layer and three distinct convolution sizes. By performing nonlinear fusion and aggregating channels from the output of the preceding layer, these modules reduce overfitting and increase the expressiveness and flexibility of the network at different sizes. Convolution kernel splitting is a method used by Inception V3 to divide large convolutions into smaller ones. A 3x3 convolution, for example, is divided into 3x1 and 1x3 convolutions. By lowering the number of parameters, this technique efficiently extracts spatial features while speeding up network training.

By the above approaches, 2071 features are extracted, of which 2048 features are obtained from Inception V3 and 23 features from Haralick and Zernike methods.

3.4. Feature Selection

An optimal set of features is selected from the extracted features, which is utilized for the classification process. A novel approach called Anaconda-based Serval Optimization (ABSO), which is a hybrid of Green Anaconda Optimization and Serval Optimization Algorithm, has been proposed.

Green Anaconda Optimization (GAO) is an algorithm in which the green anacondas (GA) are its population members. Each GA can be modeled using a vector, and the population of GAs consisting of these vectors is modeled. The initial position is randomly generated using the formula below.

$$Y = \begin{bmatrix} Y_1 \\ \vdots \\ Y_j \\ \vdots \\ Y_M \end{bmatrix}_{M\times a} = \begin{bmatrix} Y_{1,1} & \cdots & Y_{1,d} & \cdots & Y_{1,a} \\ \vdots & \ddots & \vdots & \ddots & \vdots \\ Y_{j,1} & \cdots & Y_{j,d} & \cdots & Y_{j,a} \\ \vdots & \ddots & \vdots & \ddots & \vdots \\ Y_{M,1} & \cdots & Y_{M,d} & \cdots & Y_{M,a} \end{bmatrix}_{M\times a} \quad (10)$$

$$Y_{j,d} = lb_d + rd_{j,d}(ub_d - lb_d); j = 1,2,..,M\ and\ d = 1,2,..,a \quad (11)$$

Y is the population matrix, Y_j is the j^{th} GA, M, a is the total GA, decision variables, $rd_{j,d}$ is the random values in [0,1], $lb_d and\ ub_d$ are lower and upper bounds.

The GAO can be mathematically expressed by two phases, providing exploration and exploitation in the search process.

- Phase 1: Mating (Exploration)

The members of the GAO population with a higher objective function value are considered to be the female equivalents of GA. The choice of each GA possible female mate is then determined by,

$$C_f^j = \left\{ Y_{l_j} : F_{l_j} < F_j \; and \; l_j \neq j \right\} \quad (12)$$

C_f^j is the female location set

GA locomotion is influenced by pheromone concentration (PC). The probability of selection is higher for better values of the goal function. For every GAO member, the probability of selection based on pheromone concentration is computed by,

$$P_t^j = \frac{CFF_t^j - CFF_{max}^j}{\sum_{x=1}^{x_j} CFF_x^j - CFF_{max}^j}; j = 1,2,..,M \; and \; t = 1,2,..,x_j \quad (13)$$

GA in GAO design arbitrarily chooses a potential material. To identify the selected female species for the GA, the cumulative probability function of potential females is computed and compared with a randomly generated number.

$$C_t^j = P_t^j + C_{t-1}^j \quad (14)$$

$$SF^j = C_f^j : C_{t-1}^j < r_{j,d} < C_t^j \quad (15)$$

The updated location of GA is given as,

$$y_{j,d}^{Phase1} = y_{j,d} + r_{j,d}\left(SF_d^j - I_{j,d}.y_{j,d}\right) \quad (16)$$

$$Y_j = \begin{cases} X_j^{Phase1} & ; F_j^{Phase1} < F_j \\ F_j & ; otherwise \end{cases} \quad (17)$$

$I_{j,d}$ is the random number in set (1,2).

- Phase 2: Hunting (Exploration)

An initial random position is established near each green anaconda to imitate the hunting technique and reposition population members toward approaching prey. The positions are then updated using the equations below,

$$y_{j,d}^{Phase2} = y_{j,d} + (1 - 2r_{j,d})\frac{ub_d - lb_d}{s} \quad (18)$$

$s = 1,2 \ldots, S$, Where s, S are present and the maximum iteration.

$$Y_j = \begin{cases} X_j^{Phase2} & ; F_j^{Phase1} < F_j \\ F_j & ; otherwise \end{cases} \quad (19)$$

The algorithm is repeated until the best candidate solution is recorded.

The Serval Optimization Algorithm (SOA) technique is a population-based optimizer that may provide suitable results for optimization challenges. Similar to the GAO, the vector matrix and initialization are calculated. The two phases are explained in the following section.

- Phase 1: Prey selection (Exploration)

The most desirable individual in the population is thought to be in the prey position in the SOA design. To simulate the serval's attack on the prey, the new position of the serval is first computed. The previous several positions, indicated in the following equations, are then replaced if this new location increases the value of the objective function.

$$y_{j,d}^{Phase1} = y_{j,d} + r_{j,d}\left(P_d - I_{j,d}.y_{j,d}\right) \quad (20)$$

$$Y_j = \begin{cases} X_j^{Phase1} & ; F_j^{Phase2} < F_j \\ F_j & ; otherwise \end{cases} \quad (21)$$

P_d is the prey

- Phase 2: Chase Process (Exploitation)

Inspired by several hunting behaviors, population placements are updated in the second phase of SOA to improve local search. As a result, servals in the search space will experience minor positional alterations due to the simulation of a pursuit process. The purpose is to determine a new location close to the server and replace it if it improves the objective function value in order to increase SOA's exploitation capability and discover better solutions.

$$y_{j,d}^{Phase2} = y_{j,d} + \frac{r_{j,d}(ub_d - lb_d)}{s} \quad (22)$$

$$Y_j = \begin{cases} X_j^{Phase2} & ; F_j^{Phase2} < F_j \\ F_j & ; otherwise \end{cases} \quad (23)$$

The hybrid of GAO and SOA improves the model's efficiency, achieved by providing the optimal value of GAO for initializing SOA. Ultimately, from a total of 2041 extracted features, 1045 features are selected for classification.

3.5. Classification

Using the selected features, the results are finally classified in this phase and the methods are explained in detail in the following section Figure 2 shows the Architecture of the X Fusion Strategy.

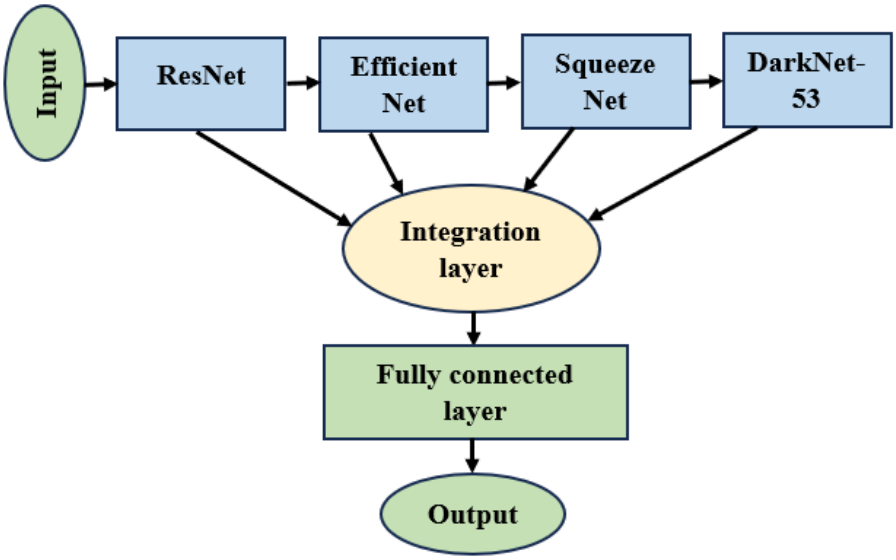

Figure 2.
X Fusion Strategy.

3.5.1. ResNet

It is well known that ResNet can train extremely deep networks without encountering the vanishing gradient issue. When training very deep neural networks, a phenomenon known as the vanishing gradient problem may occur, in which the gradients of the loss function with respect to the network weights become very small. As a result, the network may find it challenging to learn.

It employs the residual learning method to address the vanishing gradient problem. The network can learn residual mapping differences between a layer's input and output through residual learning. As a result, even very deep networks find it easier to learn the appropriate mapping. A stack of residual blocks is the standard building block for ResNets. A path is traced by two convolutional layers in each residual block. Consequently, the network can learn identity mappings, which are input-neutral mappings. This enhances the network's ability to learn residual mappings.

The identity path and skip path are the two basic paths that make up a residual block. The residual mapping, which is the difference between the desired output and the input to the block, is learned via the identity path. Bypassing the identity path, the shortcut path offers a direct connection for the input to flow through the block. The leftover block's output is provided as,

$$y = F(i) + i \tag{24}$$

Where i is Input, $F(i)$ is residual mapping learned by the block?

3.5.2. Efficient Net

The foundation of E-N Models is a straightforward and powerful compound scaling approach. Compound scaling uniformly scales each dimension with a predetermined fixed set of scaling coefficients, as opposed to arbitrarily increasing width (w), depth (d), or resolution (r). The concept behind the compound scaling approach is to scale with a constant ratio in order to balance the dimensions of width, depth, and resolution. It is essential to balance network breadth, depth, and resolution during ConvNet scaling to achieve greater accuracy and efficiency.

Due to this, E-N models are able to perform better than earlier CNNs while using fewer FLOPs (floating point operations per second) and parameters. For instance, we can employ a model with a high value of the *compound coefficient* if we need a network that is both accurate and effective. We can employ a model with a low value of the *compound coefficient* if we require a compact and effective network. Efficiency and accuracy are improved with E-N models. It is explained how a *compound coefficient* φ is used in a compound scaling approach to evenly scale network breadth, depth, and resolution.

$$\begin{cases} d = \alpha^{\varphi} \\ w = \beta^{\varphi} \\ r = \gamma^{\varphi} \end{cases} \tag{25}$$

Where $\alpha.\beta^2.\gamma^2 \approx 2; \alpha \geq 1, \beta \geq 1, \gamma \geq 1$

A modest grid search can find the constants α,β,γ. The user-specified coefficient φ determines how many more resources are available for model scaling.

3.5.3. Squeeze-Net

With two convolution layers (CL), eight fire layers, three max-pooling levels, one global average pooling layer, one SoftMax output layer, and so on, SqueezeNet is a convolutional network. SqueezeNet has 8 Fire modules (fire2–9) after the 1st CL (conv1). Finally, there is a final convolution layer. From the start of the network to its end, each Fire module has more filters than before. Max-pooling is carried out by SqueezeNet using a two-stride method following layers conv10, fire8, fire4, and conv1.

The RGB channels of the network's input (i//p) measure 227 × 227 pixels. Max pooling is used to further specialize the i//p pictures after convolution. Using 3 × 3 kernels, the convolution layer connects the limited areas and weights in the i//p volumes. Each component is independently activated as the real component by each convolution layer. Each convolution layer performs activation. It utilizes fire layers, which squeeze phase (S-p) and the expanded phase (E-p) between the convolution layers. The i//p and output (o/p) tensor scales of the fire are equal. 1 × 1 filters are used in S-p, whereas, along with the above filter, 3 × 3 are used in the E-p. The o/p is given as,

$$f(y) = \sum_{fm1=1}^{FM} \sum_{c=1}^{c} W_c^f x_c^{fm1} \quad (26)$$

Where FM, C are feature maps (fms), channels. The weighted total of the feature maps of each individual tensor is the squeeze result. Max pooling down-samples along spatial dimensions, whereas the global average pooling aggregates the class feature mappings into a single value. Multiclass probability distributions are returned by the SoftMax activation method at the output end.

3.5.4. DarkNet-53

Using successive 1x1 and 3x3 convolution layers and residuals, this network model integrates the deep Residual Network with the YOLOv2 basic feature extraction network Darknet19 [18]. This includes the convolutional layer, the Batch Normalization (BN) layer, and the Leaky ReLU layer. The output of the convolution layer is determined as,

$$x_i^m = \sum_{k \epsilon M_i} x_k^{m-1} * W_{ki}^l + b_i^l \quad (27)$$

Based on the eigenvalues of the same batch, BN is responsible for normalizing the output to the same distribution. The linear unit with leakage correction (Leaky ReLU) activation function makes the network model more nonlinear.

3.5.5. Integration Layer

The output of the above four models is integrated in this layer, and the final output is processed by where the classification is done.

3.5.6. Fully Connected Layer

It is the final layer in which the results are classified utilizing the output of the integrated layer [19].

4. Results and Discussions

Performance indicators are used to assess the outcomes based on the dataset obtained. The computed results are compared between the proposed and current models, including ResNet, EfficientNet, SqueezeNet, and DarkNet-53, by implementing them in a MATLAB platform.

4.1. Dataset Description

The dataset comprises 374 samples prepared by various pathologists taken from Kaggle. The dataset is augmented, resulting in 2620 images. It includes three types of malignant lymphoma: CLL, FL, and MCL. From H+E-stained samples, these three lymphoma forms can only be reliably and consistently identified by highly skilled pathologists [20].

4.2. Image Results

This section provides the image results obtained from the MATLAB tool for the proposed model.

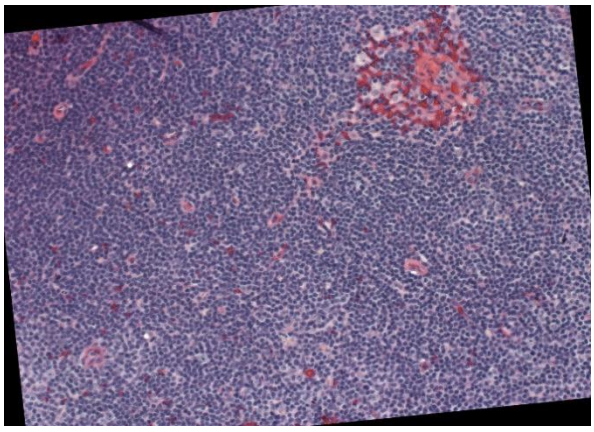

Figure 3(a).
Input image.

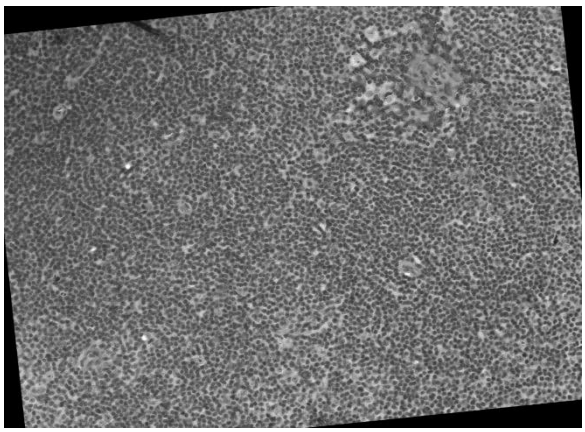

Figure 3(b).
Background correction.

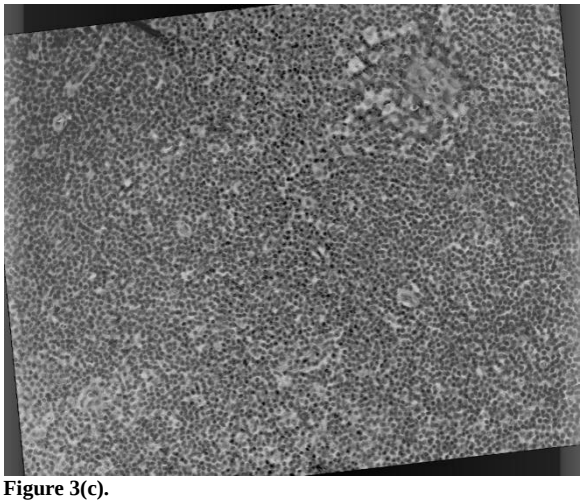

Figure 3(c).
Normalization.3.

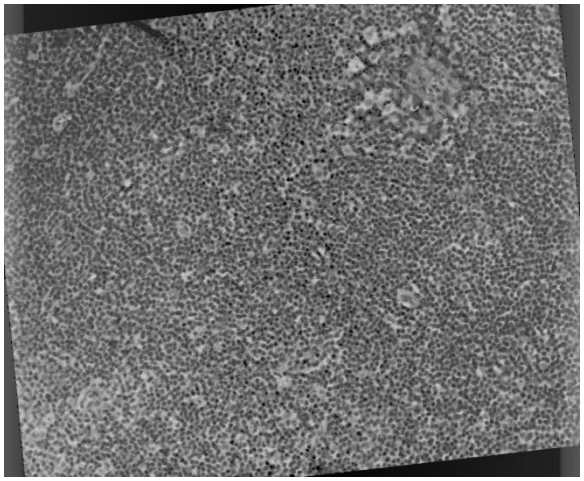

Figure 3(d).
Denoised output.

The performance metrics that are detailed below are used to evaluate both the proposed and the existing strategies. Figure 3 provides the confusion matrix, and Table 1 provides the numerical results of the models.

4.3. Performance Metrics and Analysis

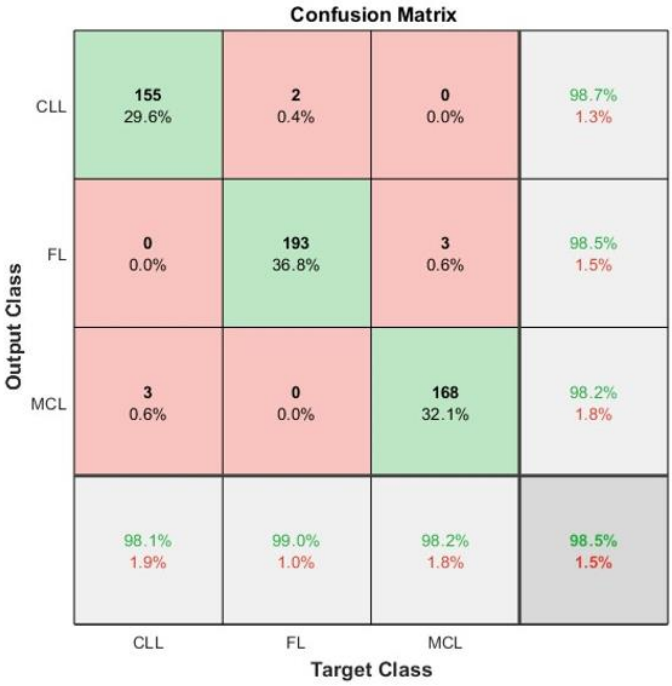

Figure 4.
Confusion matrix of the model.

Table 1.
Numerical results of the Evaluation metrics.

Model	Accuracy	Sensitivity	Specificity	Precision	F-measure	FPR	FNR	MCC
Proposed	0.9898	0.9847	0.9924	0.9847	0.9847	0.0076	0.0153	0.9771
ResNet	0.9758	0.9637	0.9819	0.9637	0.9637	0.0181	0.0363	0.9456
Squeeze Net	0.9733	0.9599	0.98	0.9599	0.9599	0.02	0.0401	0.9399
Efficient Net	0.9707	0.9561	0.9781	0.9561	0.9561	0.0219	0.0439	0.9342
Dark Net	0.9656	0.9485	0.9742	0.9485	0.9485	0.0258	0.0515	0.9227
Mobile Net	0.9517	0.9275	0.9637	0.9275	0.9275	0.0363	0.0725	0.8912

4.3.1. Accuracy

It is the ratio of accurate predictions to all observations (i/p). It is ascertained by means of (28)

$$Accuracy = \frac{correct\ predictions}{Total\ samples} \quad (28)$$

4.3.2. Precision

A performance indicator called precision indicates the proportion of a model's positive predictions that are actually accurate. To ascertain whether or not what you detect is actually there, precision is essential. It says as

$$Precision = \frac{TP}{TP+FP} \quad (29)$$

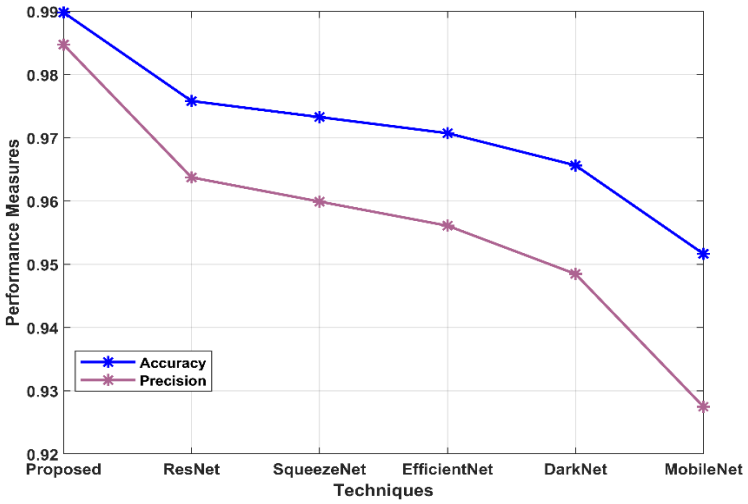

Figure 5.
Examination of models in terms of Accuracy and Precision.

Figure 5 examines the recommended methods in use with regard to accuracy and precision. From the graphical representation, it is seen that the proposed approach has a higher accuracy of 98.98% and precision of 98.47%.

4.3.3. Sensitivity

This measures the percentage of true positives that are correctly identified. It is stated as,

$$Sensitivity = \frac{TP}{TP+FN} \quad (30)$$

4.3.4. Specificity

It measures the proportion of true negatives that are correctly identified. It is computed using

$$Specificity = \frac{TN}{TN+FP} \quad (31)$$

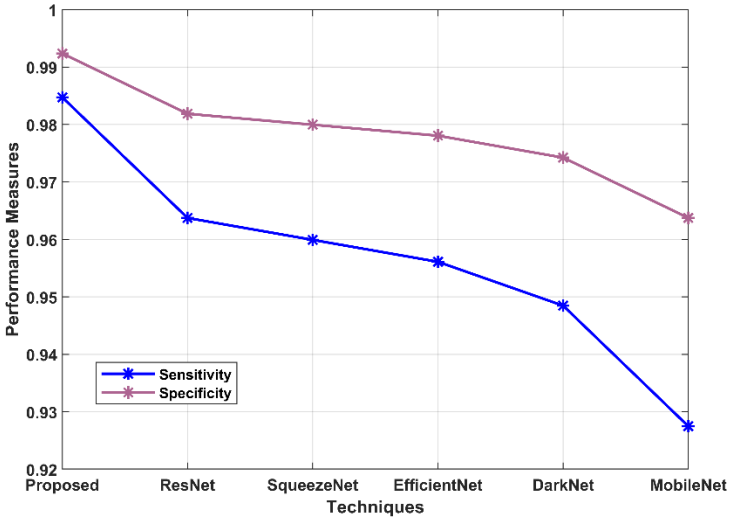

Figure 6.
Examination of models in terms of Sensitivity and Specificity.

Figure 6 examines the recommended methods in use regarding Sensitivity and Specificity. From the graphical representation, the suggested approach has a higher Sensitivity of 98.47% and a Specificity of 99.24%.

4.3.5. FPR

FPR are actually negative but predicted to be positive, which is determined by,

$$FPR = \frac{FP}{FP+TN} \quad (32)$$

4.3.6. FNR

FNR are actually positive but predicted to be negative, which is determined by,

$$FNR = \frac{FN}{FN+TP} \quad (33)$$

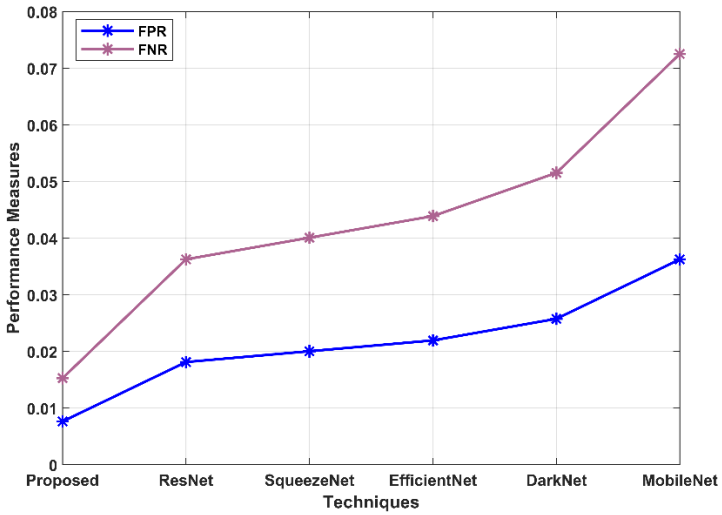

Figure 7.
Suggested and existing models in terms of FPR and FNR.

Figure 7 examines the recommended methods in use regarding F1-score and MCC. From the graphical representation, the proposed model has a lower FPR of 0.76% and an FNR of 1.53%.

4.3.7. F Measure

Precision and recall are combined to create a composite statistic that serves as a general performance evaluation score. It is expressed as

$$F\ measure = 2 * \frac{Precision * Recall}{Precision + Recall} \quad (34)$$

4.3.8. Mathew's Correlation Coefficient (MCC)

The degree of correlation between the predicted and actual outcomes is measured by MCC. It's expressed as,

$$MCC = \frac{(TP \times TN) - (FP \times FN)}{\sqrt{(TP+FP)(TP+FN)(TN+FP)(TN+FN)}} \quad (35)$$

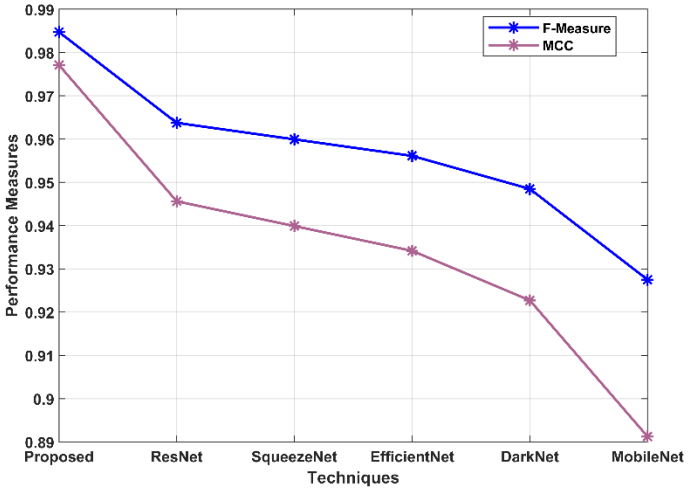

Figure 8.
Examination of models in terms of F-measure and MCC.

Figure 8 examines the recommended methods in use regarding F1-score and MCC. From the graphical representation, it is seen that the recommended approach has a higher F1-score of 98.47% and MCC of 97.71%.

5. Conclusion

Lymphomas are a substantial risk to healthcare and are the fourth most prevalent type of cancer in both men and women. Due to erroneous illness detsection, this particular type of cancer has also contributed to increased death rates. A new method for DNA microarray analysis, called a Hybrid modified RCNN-based ROI identification and Spot Detect-X fusion strategy, is proposed to overcome the limitations of current techniques. The data is first pre-processed using a variety of methods, including improved median filter noise reduction, image augmentation, normalization, and background correction. The modified RCNN is used for ROI identification. The features are then extracted, and the hybrid Anaconda-based Serval optimization is used to select the features. Lastly, the Spot Detect-X Fusion Strategy is employed to classify the illnesses. When the recommended model was used in a MATLAB platform, its accuracy was 98.98%, sensitivity

98.47%, specificity 99.24%, precision 98.47%, F-measure 98.47%, FPR and FNR of 0.76% and 1.53%, and MCC of 97.71%. Therefore, it is demonstrated that the suggested model performs better than the current techniques.

References

[1] Z. Lu *et al.*, "Deep-learning–based characterization of tumor-infiltrating lymphocytes in breast cancers from histopathology images and multiomics data," *JCO Clinical Cancer Informatics*, vol. 4, pp. 480-490, 2020. https://doi.org/10.1200/CCI.19.00126

[2] D. Ennishi, E. D. Hsi, C. Steidl, and D. W. Scott, "Toward a new molecular taxonomy of diffuse large B-cell lymphoma," *Cancer Discovery*, vol. 10, no. 9, pp. 1267-1281, 2020.

[3] V. P. Wagner *et al.*, "Mantle cell lymphoma, malt lymphoma, small lymphocytic lymphoma, and follicular lymphoma of the oral cavity: An update," *Journal of Oral Pathology & Medicine*, vol. 50, no. 6, pp. 622-630, 2021. https://doi.org/10.1111/jop.13214

[4] W. Zhang *et al.*, "A novel diagnostic approach for the classification of small B-cell lymphoid neoplasms based on the NanoString platform," *Modern Pathology*, vol. 35, no. 5, pp. 632-639, 2022. https://doi.org/10.1038/s41379-021-00954-z

[5] M. Elhadary *et al.*, "Revolutionizing chronic lymphocytic leukemia diagnosis: A deep dive into the diverse applications of machine learning," *Blood Reviews*, vol. 62, p. 101134, 2023. https://doi.org/10.1016/j.blre.2023.101134

[6] M. M. Bühler, J. I. Martin-Subero, Q. Pan-Hammarström, E. Campo, and R. Rosenquist, "Towards precision medicine in lymphoid malignancies," *Journal of Internal Medicine*, vol. 292, no. 2, pp. 221-242, 2022. https://doi.org/10.1111/joim.13423

[7] S. Kesavan and N. H., "Microarray based geonomic biomarker optimization for cancer prognosis," presented at the Second International Conference on Electronics and Renewable Systems (ICEARS), 2023.

[8] H. L. Bhavyashree, C. R. Nagarathna, A. Preetham, and R. Priyanka, "Modified cluster based certificate blocking of misbehaving node in MANETS," presented at the 1st International Conference On Advanced Technologies In Intelligent Control, Environment, Computing & Communication Engineering (ICATIECE), 2019.

[9] E. Wulczyn *et al.*, "Deep learning-based survival prediction for multiple cancer types using histopathology images," *PloS One*, vol. 15, no. 6, p. e0233678, 2020. https://doi.org/10.1371/journal.pone.0233678

[10] A. Echle, N. T. Rindtorff, T. J. Brinker, T. Luedde, A. T. Pearson, and J. N. Kather, "Deep learning in cancer pathology: A new generation of clinical biomarkers," *British Journal of Cancer*, vol. 124, no. 4, pp. 686-696, 2021. https://doi.org/10.1038/s41416-020-01122-x

[11] X. Zhao *et al.*, "Deep learning–based fully automated detection and segmentation of lymph nodes on multiparametric-mri for rectal cancer: A multicentre study," *EBioMedicine*, vol. 56, p. 102780, 2020. https://doi.org/10.1016/j.ebiom.2020.102780

[12] S. Chandana, C. R. Nagarathna, A. Amrutha, and A. Jayasri, "Detection of image forgery using error level analysis," presented at the International Conference on Intelligent and Innovative Technologies in Computing, Electrical and Electronics (IITCEE), 2024.

[13] A. R. Colombo *et al.*, "Single-cell spatial analysis of tumor immune architecture in diffuse large B-cell lymphoma," *Blood Advances*, vol. 6, no. 16, pp. 4675-4690, 2022. https://doi.org/10.1182/bloodadvances.2022007493

[14] C. Nagarathna and M. Kusuma, "Early detection of Alzheimer's disease using MRI images and deep learning techniques," *Alzheimer's & Dementia*, vol. 19, p. e062076, 2023. https://doi.org/10.1002/alz.062076

[15] I. M. Coleman *et al.*, "Therapeutic implications for intrinsic phenotype classification of metastatic castration-resistant prostate cancer," *Clinical Cancer Research*, vol. 28, no. 14, pp. 3127-3140, 2022. https://doi.org/10.1158/1078-0432.CCR-21-4289

[16] A. Preetham, S. Vyas, M. Kumar, and S. N. P. Kumar, "Optimized convolutional neural network for land cover classification via improved lion algorithm," *Transactions in GIS*, vol. 28, no. 4, pp. 769-789, 2024. https://doi.org/10.1111/tgis.13150

[17] A. Preetham and V. V. Battu, "Soil moisture retrieval using sail squirrel search optimization-based deep convolutional neural network with sentinel-1 Images," *International Journal of Image and Graphics*, vol. 23, no. 05, p. 2350048, 2023.

[18] C. Nagarathna, A. Jayasri, S. Chandana, and A. Amrutha, "Identification of image forgeries using machine learning-a review," *Journal of Innovative Image Processing*, vol. 5, no. 3, pp. 323-336, 2023. https://doi.org/10.36548/jiip.2023.3.007

[19] U. Mahanthesha, R. Tejaswini, and C. Nagarathna, "Face recognition using MTCNN, inception-resnet with ensemble approach," presented at the International Conference on Intelligent and Innovative Technologies in Computing, Electrical and Electronics (IITCEE), 2025.

[20] N. C. Rangegowda, K. Mohanchandra, A. Preetham, M. Almas, and H. Huliyappa, "A multi-layer perceptron network-based model for classifying stages of Alzheimer's disease using clinical data," *Revue d'Intelligence Artificielle*, vol. 37, no. 3, p. 601, 2023. https://doi.org/10.18280/ria.370309